



Bipolar charge transport in a robust hexacoordinate organosilane

Adam W. Earnhardt^a, Kevin M. Boyle^b, Tyler Adams^c, Michael G. Walter^{a,c}, Yizhou Wang^c, Yong Zhang^{c,d}, Adesola Adeyemi^c, Jon Merkert^{a,c}, Askhat N. Bimukhanov^e, Anuar A. Aldongarov^{e,f}, Colin D. McMillen^g, Thomas A. Schmedake^{a,c,*}

^a Department of Chemistry, University of North Carolina at Charlotte, Charlotte NC 28223, USA^b Margik, Burson 255, 9201 University City Blvd, Charlotte, NC 28223, USA^c Nanoscale Science Program, University of North Carolina at Charlotte, Charlotte, NC 28223, USA^d Department of Electrical and Computer Engineering, University of North Carolina at Charlotte, Charlotte NC 28223, USA^e Department of Technical Physics, Faculty of Physics and Technology, L.N. Gumilyov Eurasian National University, Nur-Sultan, Kazakhstan^f Laboratory of Physical and Quantum Chemistry, L.N. Gumilyov Eurasian National University, Nur-Sultan, Kazakhstan^g Department of Chemistry, Clemson University, Clemson, SC 29634, USA

ARTICLE INFO

Article history:

Received 15 September 2021

Revised 30 November 2021

Accepted 6 December 2021

Available online 12 December 2021

Keyword:

Hexacoordinate silicon

Organosilicon

Hypercoordinate

Bipolar charge transfer

Organic electronics

ABSTRACT

A hexacoordinate organosilane with a SiC₄N₂ skeleton has been synthesized from the reaction of a tridentate, dianionic, CNC-diphenylpyridine (DPP) ligand with SiCl₄. The complex has a distorted octahedral geometry with short Si–N bond lengths averaging 1.9111(14) Å. The Si(DPP)₂ complex is resistant to hydrolysis and thermally robust. Thermally evaporated films of Si(DPP)₂ exhibit bipolar charge transport, with electron and hole charge mobilities high enough for device applications ($\mu_e = 18 \times 10^{-5}$ cm²V⁻¹s⁻¹ and $\mu_h = 1.1 \times 10^{-5}$ cm²V⁻¹s⁻¹). Computational modeling indicates electron transport involves a conventional π -delocalized LUMO, but that hole transport involves a delocalized σ -bonded HOMO.

© 2021 Elsevier B.V. All rights reserved.

1. Introduction

While the vast majority of silicon-containing compounds possess tetracoordinate silicon atoms, there are several notable examples of stable, robust pentacoordinate and hexacoordinate silicon species. The work of Voronkov and others with silatranes is particularly relevant in this regard [1–6]. The silatranes with an SiO₃NX skeleton and a sterically constrained transannular N–Si bond are an important class of pentacoordinate silanes that have been explored for a wide range of applications including immobilization of biomolecules [7], cross-coupling reactions [8], and hair-growth and pharmacological applications [9,10]. The silicon porphyrins [11] and phthalocyanines with an SiN₄X₂ skeleton are another significant class of hypercoordinate silicon complexes that have been explored for biological [12–17] and energy-related applications [18–24]. In both cases, incorporation of the formally neutral, nitrogen base sites within a polydentate ligand framework prevents dissociation

and imparts the moisture and thermal stability necessary for many applications (Fig. 1).

By contrast, hypercoordinate organosilanes with hemilabile CN-bidentate ligands or NCN tridentate ligands where the neutral nitrogen donor site is not constrained possess weak, long range Si–N interactions at most [25–27]. Consequently, structural studies of the SiC₄N₂ skeleton are quite rare. The Cambridge Structural Database contains only one hit for a SiC₄N₂ skeleton with intramolecular Si–N bonds of 3 Å length or less (Fig. 2),[28] and no hits for a SiC₄N₂ skeleton with Si–N bond lengths approaching a conventional Si–N bond length of 2.0 Å or less. The potential for exploiting Voronkov's strategy of a sterically constrained N–Si transannular interaction in stabilizing higher coordination numbers for organosilicon complexes becomes readily apparent and suggests CNC-pincer ligands may be attractive ligands for developing the SiC₄N₂ framework.

We previously exploited a similar strategy to develop Si(pincer)₂ complexes as attractive candidates for organic electronic applications including OLED, OPV, and OFETs since they are thermally robust, redox-active, non-polar, and electronically tunable through synthetic modification. In addition, the silicon center with its perpendicular ligands creates a site of tortuosity, a desirable feature for raising the T_g of organic materials for

* Dedicated to Mikhail Grigorievich Voronkov in celebration of the 100th anniversary of his birth.

* Corresponding author: Department of Chemistry, University of North Carolina at Charlotte, Charlotte NC 28223, USA.

E-mail address: Tom.Schmedake@uncc.edu (T.A. Schmedake).

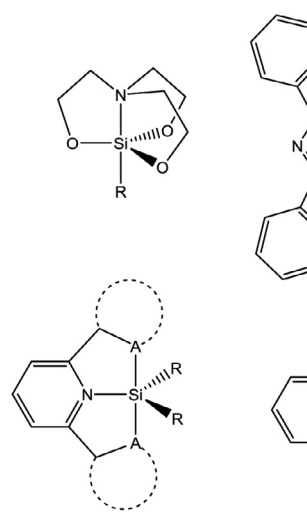


Fig. 1. N-Si transannular interactions in silatranes and silicon phthalocyanine complexes (top row), and the pyridine-containing pincer ligands explored in this manuscript (bottom row).

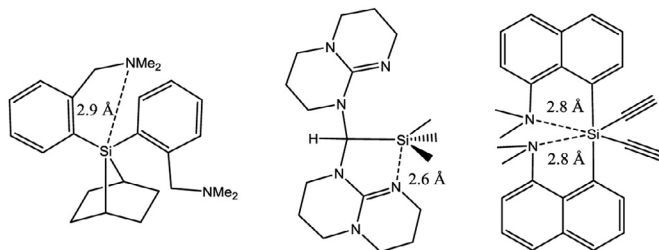
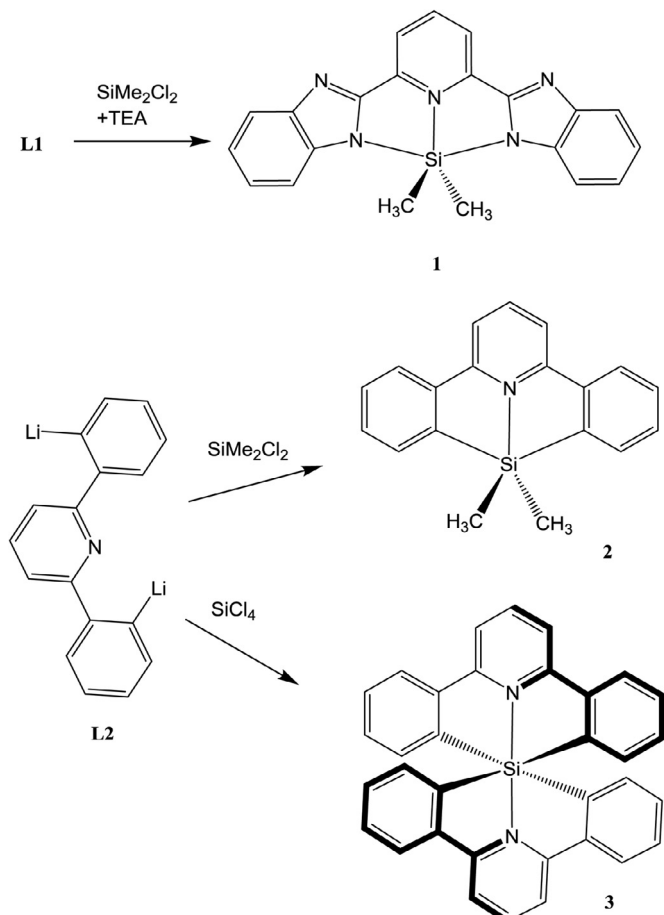


Fig. 2. Structurally determined hypercoordinate silicon compounds with SiC₄N₁ or SiC₄N₂ frameworks reported in the Cambridge Structural Database [28,29,30].

electronic applications. The redox innocence of the silicon center leads to delocalized, ligand-localized redox events [31], lowering the reorganization energies and improving charge mobilities. In previous studies, we focused on hexacoordinate silicon complexes with a SiN₆ framework [32]. These nitrogen-rich complexes possessed a low LUMO and demonstrated effectiveness as an electron transport/hole blocking material. Recent developments in single-layer OLEDs have demonstrated a need for the development of robust, bipolar transport materials (electron and hole transport) for triplet-harvesting dopants [33–35]. In this manuscript, we turn our focus towards the development of Si(pincer)₂ complexes as bipolar hosts with the development of a robust SiC₄N₂ Si(pincer)₂ complex.

2. Results and discussion

In our initial attempts to develop hypercoordinate organosilanes with pincer ligands, we attempted to synthesize the pentacoordinate species, Si(bzimpy)Me₂, **1**, and Si(DPP)Me₂, **2** (DPP = 2,6-diphenylpyridine ligand, Scheme 1). The reaction of the ligand 2,6-bis(benzimidazol-2-yl)pyridine (bzimpy, **L1**), with SiMe₂Cl₂ in chloroform with triethylamine as an HCl scavenger produces complex **1**. The reaction of 2,6-bis(2-bromophenyl)pyridine with n-BuLi in THF at -78 °C generates the dianion, **L2**, which was subsequently combined with SiMe₂Cl₂ in an attempt to generate **2**. MALDI mass spectroscopy provided evidence that both species were obtained though neither was stable enough to be isolated and purified. In addition, both species possess a ²⁹Si NMR signal consistent with a pentacoordinate silicon center: -74 ppm (compound **1**) and -72 ppm (compound **2**). We were able to ob-



Scheme 1. Synthesis of compounds **1**-**3**.

tain crystals of **1**, by taking advantage of the fact that hydrolysis/solvolytic of **1** regenerates **L1**. So combination of **L1** with an excess of SiMe₂Cl₂ in CHCl₃ and an excess of triethylamine produced crystals of **1** that could be briefly manipulated under mineral oil and immediately mounted under the cryostream at -100 °C (Fig. 3). Likewise, by addition of an excess of SiMe₂Cl₂ to **L1**, we were able to obtain ¹H and ¹³C spectra for **1** (ESI). However, we were unable to produce samples of **2** of sufficient purity for assignment of ¹H and ¹³C. The poor stability of **1** and **2** is consistent with earlier observations by Jia and coworkers, who despite success isolating heavier Group IV congeners reported that the complexes Si(bip)Ph₂ and Si(bap)Ph₂ were thermally unstable and underwent rapid decomposition upon isolation at ambient temperature (bip = 2,6-bis(2'-indolyl)pyridine and bap = 2,6-bis[2'-(7-azaindolyl)]pyridine) [36].

The crystal structure of **1** indicates a pentacoordinate silicon center with a SiC₂N₃ skeleton, with a planar bzimpy ligand and a distorted trigonal bipyramidal geometry at silicon with the pyridine and methyl substituents occupying the equatorial plane ($\angle C20\text{-Si-C}21 = 122.25(7)^\circ$, $\angle C20\text{-Si-N}3 = 120.25(6)^\circ$, and $\angle C21\text{-Si-N}3 = 117.50(6)^\circ$) and the benzimidazole substituents occupying distorted axial positions ($\angle N5\text{-Si-N}1 = 159.28^\circ$). The short transannular N3-Si bond 1.9085(13) Å is identical to the other two Si-N bonds (1.9065(13) Å and 1.9085(13) Å), a consequence of the steric constraint resulting from the NNN-pincer geometry.

The reaction of **L2** with SiCl₄ in THF at -78 °C produced the desired hexacoordinate SiC₄N₂ complex, **3**. The yields for this reaction were consistently low, with our highest yield being 17%. Nevertheless, **3** shows remarkable stability. ¹H-NMR of **3** is consis-

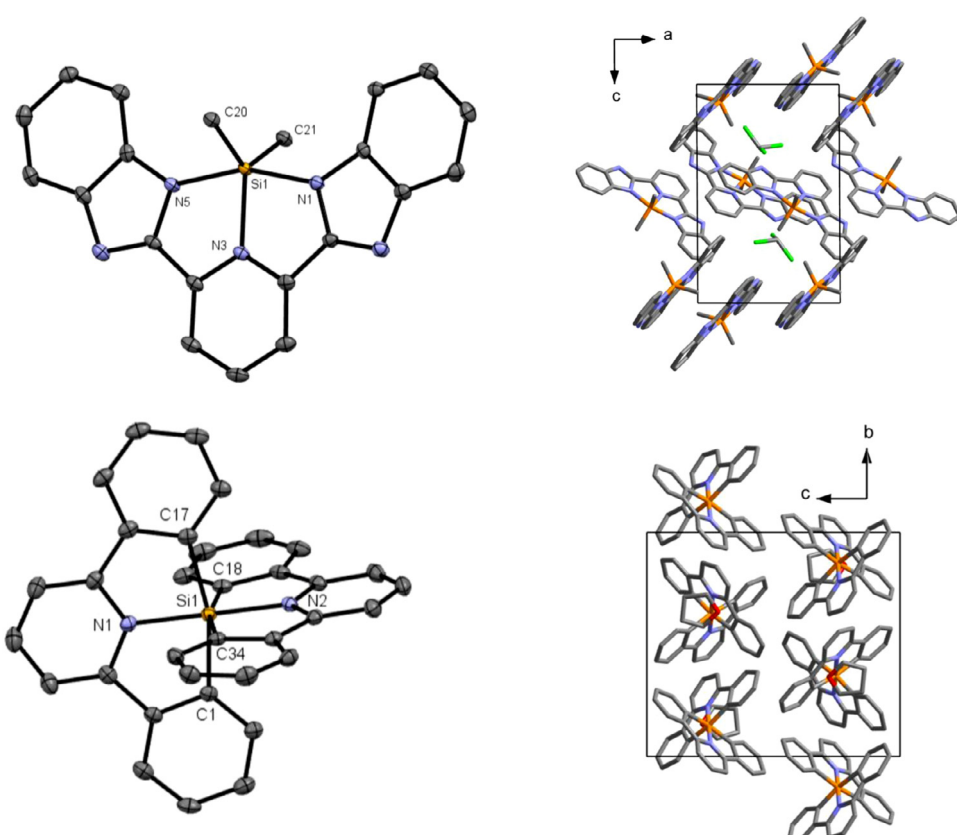


Fig. 3. (top) Crystal structure of **1**, as **1·½CHCl₃** in space group $P\bar{1}$ shown as 50% probability ellipsoids with hydrogen atoms and solvent molecules (CHCl₃) omitted for clarity, and the packing diagram of **1·½CHCl₃** with solvent included. (bottom) Crystal structure of **3**, as **3·THF** in space group $P2_1/n$ shown as 50% probability ellipsoids with hydrogen atoms and solvent molecules omitted, and the packing diagram of **3·THF**.

tent with the expected D₂d symmetry including a significant up-field shift of one of the aromatic peaks to 6.0 ppm due to shielding from the aromatic ring current of the pyridine rings. In addition, ²⁹Si-NMR gives a peak at -150 ppm, clear evidence of a well-shielded hexacoordinate silicon complex in solution. X-ray quality crystals of **3** were obtained from THF (**3·THF**, Fig. 3) and also from CHCl₃ (**3·CHCl₃**, ESI). The hexacoordinate silicon center adopts a distorted octahedral geometry with nearly planar ligands oriented perpendicular to one another. As with **1**, the Si-N bond is within normal Si-N bonding distances Si1-N1=1.9095(14) Å and Si1-N2 = 1.9126(14) Å. The four Si-C bonds are also within conventional Si-C bond lengths at just under 1.97 Å.

Unlike the pentacoordinate species, **3** is remarkably robust. Thermogravimetric analysis indicates **3** is thermally stable to over 400 °C in nitrogen (ESI). In addition, differential scanning calorimetry indicates that **3** possess a very high T_g (T_g onset = 263 °C, ESI). It is also indefinitely stable in a 50:50 mixture of DMSO and water, showing no sign of hydrolysis after 48 h. The yellow appearance of **3** is consistent with a broad low intensity absorbance centered around 420 nm (Fig. 4). Compound **3** also exhibits a weak emission in solution centered around 440 nm with a quantum yield of 0.0018 (± 0.001). The small Stokes shift may contribute to the weak fluorescence intensity observed. Attempts to measure the fluorescence lifetime of **3** in CH₂Cl₂ indicated a rapid multi-exponential decay (Fig. 5) that could be fit with a three-exponent model with an amplitude averaged lifetime of 1.6 ns (calculated as amplitude average lifetime, $\tau_a = \sum(A_n\tau_n)/\sum A_n$, with $\tau_1 = 0.50$ ns, $\tau_2 = 1.5$ ns, $\tau_3 = 6.1$ ns and respective relative amplitudes $A_1 = 0.4517$, $A_2 = 0.4229$, $A_3 = 0.1254$).

Raman spectroscopy was performed on crystals of **3·THF** (Fig. 6). The experimentally observed spectrum reasonably

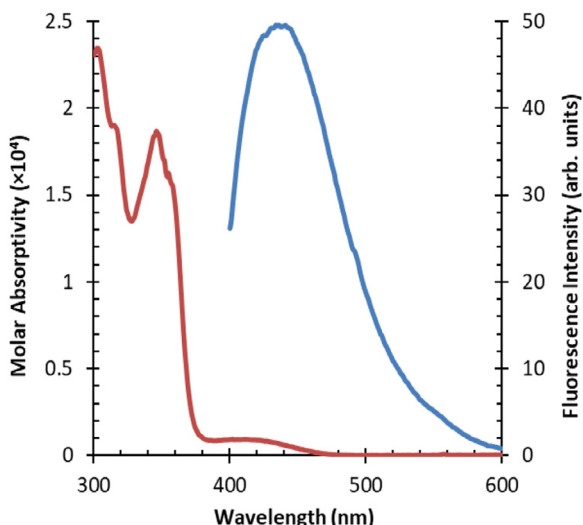


Fig. 4. UV-vis (red) and fluorescence (blue) spectra of **3** in CH₂Cl₂. Fluorescence spectrum excited at 360 nm. Caption: (For interpretation of the references to color in this figure legend, the reader is referred to the web version of this article).

matched the predicted Raman spectrum calculated for **3** in the gas phase (B3LYP/6-31G*). The strongest band in the experimental spectrum shows up at 1043 cm⁻¹ and matches the 1050 cm⁻¹ band in the theoretical spectrum that corresponds to the symmetric stretch of the SiC₄N₂ skeleton and provides a potential signature for identification of future SiC₄N₂ complexes. In addition, the close match between the experimental and theoreti-

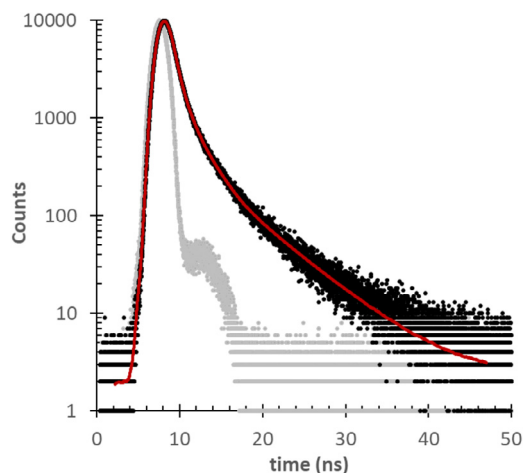


Fig. 5. Fluorescence lifetime of **3** in CH_2Cl_2 (black) fit to a three-exponential decay curve (red). Instrument response function is shown in gray. Caption: (For interpretation of the references to color in this figure legend, the reader is referred to the web version of this article).

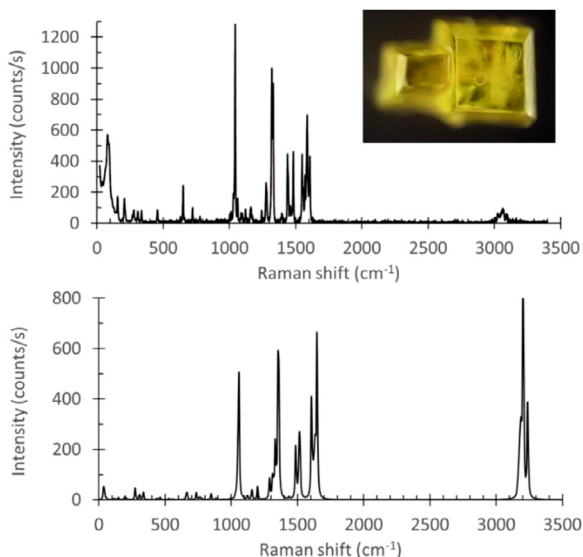


Fig. 6. Raman spectrum of $\text{Si}(\text{DPP})_2 \cdot \text{THF}$ crystals (top) and predicted Raman spectrum calculated from optimized structure of $\text{Si}(\text{DPP})_2$ in the gas phase (B3LYP/6-31G*).

cal spectra provides evidence of the accuracy of our computational modeling.

A reduction wave and an oxidation wave ($E_{\text{ox},\text{onset}} = +0.47$ V and $E_{\text{red},\text{onset}} = -2.20$ V vs. $\text{Fc}^{+/\text{0}}$, both only partially reversible) were observed in cyclic voltammetry of **3** in DMSO with TBAPF₆ and Pt electrode. These values provide a $E(\text{HOMO}) = -5.27$ V and $E(\text{LUMO}) = -2.60$ V (calculated using $E(\text{LUMO/HOMO}) = -e[\text{E}_{\text{red}/\text{ox},\text{onset}} + 4.8 \text{ V}]$). The resulting band gap $\Delta E_{\text{LUMO-HOMO}} = 2.73$ V is consistent with the optical band gap estimated from the edge of the low-energy absorption band at 2.7 eV. As expected, switching from N-rich bzimpy ligand to the diphenylpyridine ligand raised the HOMO and LUMO considerably. By comparison, $\text{Si}(\text{bzimpy})_2$ has an $E(\text{LUMO}) = -3.4$ V based on CV and an estimated $E(\text{HOMO})$ of -5.9 V based on an optical band gap of 2.5 eV.

Samples of **3** were transferred to a glove box equipped with a thermal evaporation system to explore the charge transport properties of a thin film. Electron only devices were constructed by evaporating and depositing a thin layer of **3** (180 nm) onto an

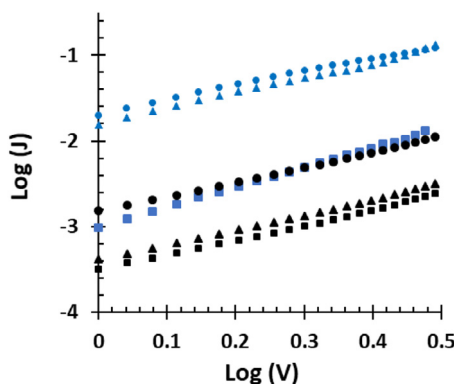


Fig. 7. Charge mobility curves for $\text{Si}(\text{DPP})_2$ thin films plotted as $\text{Log}(\text{Voltage}, V)$ vs. $\text{Log}(\text{current density}, J$) measured in units of A/cm^2 for three best-performing hole mobility devices (black) and electron mobility devices (blue) in the space-charge-limited region. The surface area for all films was $6.0 \times 10^{-6} \text{ m}^2$. The film thickness for $\text{Si}(\text{DPP})_2$ was 173 nm for hole mobility devices and 180 nm for electron mobility devices.

Table 1
Calculated and experimental charge mobility data for $\text{Si}(\text{DPP})_2$ films.

	h^+	e^-
$\lambda_{\text{calc(h/e)}}$	248 meV	345 meV
$V_{\text{calc(h/e)}}$	0.14 meV	2.0 meV
$\mu_{\text{calc(h/e)}}$	$3.5 \times 10^{-5} \text{ cm}^2 \text{V}^{-1} \text{s}^{-1}$	$8.8 \times 10^{-5} \text{ cm}^2 \text{V}^{-1} \text{s}^{-1}$
$\mu_{\text{exp(h/e)}}$	$1.1 \times 10^{-5} \text{ cm}^2 \text{V}^{-1} \text{s}^{-1}$ (st.dev.) $(0.92 \times 10^{-5} \text{ cm}^2 \text{V}^{-1} \text{s}^{-1})$	$18 \times 10^{-5} \text{ cm}^2 \text{V}^{-1} \text{s}^{-1}$ $(11 \times 10^{-5} \text{ cm}^2 \text{V}^{-1} \text{s}^{-1})$

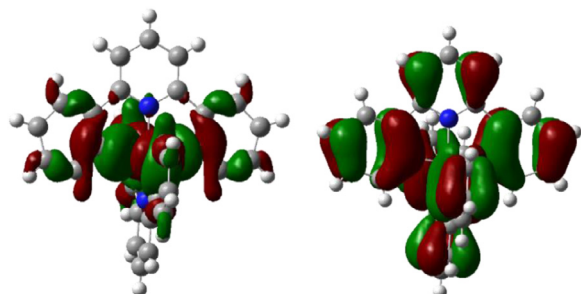


Fig. 8. HOMO (left) and LUMO (right) of $\text{Si}(\text{DPP})_2$.

ITO surface followed by aluminum. For the hole only devices, **3** (173 nm) was deposited on ITO/PEDOT:PSS followed by gold. $\text{Log}(J)\text{-log}(V)$ plots were used to confirm the devices were operating in a space-charge limited current regime (Fig. 7), and the leading three electron only and hole only devices were averaged to give an electron mobility of $\mu_e = 18 \times 10^{-5} \text{ cm}^2 \text{V}^{-1} \text{s}^{-1}$ and $\mu_h = 1.1 \times 10^{-5} \text{ cm}^2 \text{V}^{-1} \text{s}^{-1}$ (Table 1).

We used computational modeling to probe the electronic structure and to better understand the bipolar charge transport of **3** and why the electron mobility is higher than the hole mobility in **3**. The geometry of $\text{Si}(\text{DPP})_2$ was optimized using DFT calculations, (B3LYP/6-31G*, Gaussian 16). The resulting HOMO has an unusual delocalized σ -orbital symmetry around the SiC_4 plane (Fig. 8). The LUMO by contrast is a more conventional delocalized pi-orbital spread out over the entire molecule. Electron and hole mobilities were estimated using Marcus-Hush theory, and the Marcus equation with $\Delta G^\circ = 0$ was used to measure the rate of charge transfer (Eqs. (1)–(6)), [37,38]. To estimate the electronic coupling (tunneling matrix) $V_{\text{h/e}}$, the method of energy splitting in dimer was used with Koopman's theorem (KT-ESD method). Neighboring $\text{Si}(\text{DPP})_2$ molecules in the crystal lattice related through an inversion center were selected for a single point energy calculation to ensure frontier orbital splitting was exclusively a result of electronic cou-

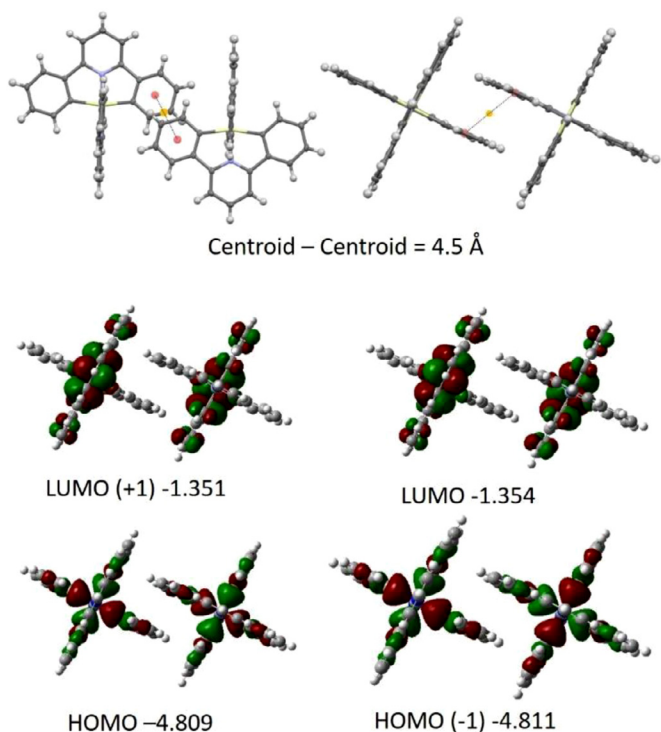


Fig. 9. Structure of neutral symmetrical dimer from crystal structure of $\text{Si}(\text{DPP})_2 \cdot \text{THF}$ lattice (top). Orange dot indicates a crystallographic inversion center, red dots indicate calculated centroids of the phenyl rings. Calculated frontier orbitals and energy levels (eV) of neutral dimers (bottom).

pling and not due to differences in site energy (Fig. 9). The hole transport is significantly hindered by poor electronic coupling resulting from the poor overlap of the σ -delocalized HOMO/HOMO-1 orbitals, but the LUMO/LUMO+1 orbital splitting is only marginally better. Also, the considerably lower hole reorganization energy somewhat offsets the difference and results in calculated charge carrier rates that are relatively matched with each other and with the experimentally observed rates.

$$K_{h/e} = \left(\frac{\pi}{\lambda_{h/e} k_B T} \right)^{1/2} \times \frac{V_{h/e}^2}{\hbar} \times \exp\left(\frac{-\lambda_{h/e}}{4k_B T} \right) \quad (1)$$

$$\lambda_{hole} = [\mathbf{E}^+(\mathbf{A}) + \mathbf{E}(\mathbf{A}^+)] - [\mathbf{E}^+(\mathbf{A}^+) + \mathbf{E}(\mathbf{A})] \quad (2)$$

$$\lambda_{electron} = [\mathbf{E}^-(\mathbf{A}) + \mathbf{E}(\mathbf{A}^-)] - [\mathbf{E}^-(\mathbf{A}^-) + \mathbf{E}(\mathbf{A})] \quad (3)$$

$$V_{h/e} = \frac{E_{HOMO/LUMO+1} - E_{HOMO-1/LUMO}}{2} \quad (4)$$

$$D = 0.5kr^2 \quad (5)$$

$$\mu = eD/k_B T \quad (6)$$

3. Conclusion

The current synthetic route proceeds through initial formation of the dilithio dianion of the CNC ligand. This greatly limits the synthetic versatility of the method, precluding benzylic hydrogens or other acidic sites for example. In addition, the overall yield was consistently low in our hands. Continued development of ortho-selective C–H silylation methods, could be very beneficial for increasing the availability and synthetic variability of $\text{Si}(\text{CNC})_2$ complexes [39,40].

Nevertheless, the robustness of $\text{Si}(\text{DPP})_2$ demonstrates the feasibility of employing dianionic CNC-pincer ligands for stabilizing hexacoordinate silicon complexes. Hole mobility via intermolecular hopping involving a sigma-delocalized HOMO is about an order of magnitude lower than electron mobility involving the pi-delocalized LUMO. This suggests $\text{Si}(\text{DPP})_2$ and other $\text{Si}(\text{CNC})_2$ complexes may be attractive targets for bipolar charge transport for single-layer OLEDs and other organic electronic devices, and further synthetic development of $\text{Si}(\text{CNC})_2$ complexes is warranted.

4. Experimental

General – Tetrahydrofuran was distilled from a benzophenone–sodium still prior to use. **L1** and all other reagents were purchased and used without further purification. **L2** was synthesized and purified following a previously reported Suzuki-coupling method [41].

Attempted synthesis of **1**. 2,6-bis(benzimidazol-2-yl)pyridine (**L1**, 0.20 mmol, 62 mg) was added to an NMR tube with 1 mL of CDCl_3 . Excess triethylamine (100 μL , 0.72 mmol) was added to the NMR tube, and the tube was flushed with nitrogen. Dichlorodimethylsilane (100 μL , 0.82 mmol) was then injected. Crystals of **1** formed in the NMR tube. Contents of the NMR tube were poured into a Petri dish containing mineral oil, an appropriate crystal was quickly mounted on a nylon-loop goniometer head and placed in the cryostream to obtain the x-ray crystal structure. ^1H NMR (CDCl_3 , 500 MHz): δ (ppm, relative to TMS) = 0.90 (S, 3H), 7.30 (ddd, 2H, 8.0 Hz, 7.1 Hz, 1.4 Hz) 7.36 (ddd, 2H, 8.0 Hz, 7.7 Hz, 1 Hz) 7.68 (d, 2H, 7.8 Hz), 7.84 (d, 2H, 7.8 Hz), 8.29 (d, 2H, 7.7 Hz), 8.39 ppm (M, 1H). $^{13}\text{C}\{^1\text{H}\}$ NMR (CDCl_3 , 125 MHz): δ (ppm relative to TMS) = 5.4, 113.9, 118.7, 121.0, 123.1, 124.6, 137.9, 147.2, 148.1, 148.8, 149.6. ^{29}Si NMR (CDCl_3 , 99 MHz): δ (ppm relative to TMS) = −73.6. MS (MALDI-TOF): [M–H]⁺, m/z = 368.8.

Attempted synthesis of **2**. 2,6-bis(2-bromophenyl)pyridine (0.112 g) was placed into a dry Schlenk flask with a stir bar. The flask was degassed and THF (~50 mL) was added. The solution was placed under nitrogen and stirred in a dry ice/acetone bath for 10 min. Then n-BuLi (0.253 mL, 2.2 equiv) was added to the flask and stirred for an additional 30 min. The solution turned a dark brown/rusty color upon addition. Dichlorodimethylsilane (0.040 mL, 1 equiv) was added to the flask and stirred. The solution was left to slowly warm to room temperature overnight. ^{29}Si NMR (CD_2Cl_2 , 99 MHz): δ (ppm relative to TMS) = −71.8. MS (MALDI-TOF): [M(−CH₃)⁺], m/z = 272.8; [M]⁺, m/z = 288.8.

Synthesis of **3**. 2,6-bis(2-bromophenyl)pyridine (1.22 g, 3.14 mmol) was added to a dry Schlenk flask with a stir bar. Tetrahydrofuran (100 mL) was added to the flask, and the resulting solution was degassed with nitrogen. The solution was stirred and cooled to −90 °C, this temperature was maintained for the duration of the reaction. 2.1 equivalents of n-BuLi (6.58 mmol, 2.65 mL of 2.5 M in hexanes solution) was added. Debromination was followed by testing aliquots from the reaction with GCMS. Upon completion of the debromination, neat SiCl_4 (0.5 eq., 1.57 mmol, 0.18 mL) was injected and stirred. The reaction solution was maintained at −90 °C for an additional hour after injection and then left to warm slowly overnight. The solvent was removed the following morning. The resulting crude material was redissolved in 400 mL of boiling THF, filtered and run through a short silica gel column (mobile phase: THF, 70–230 mesh). The solution was then evaporated on a rotary evaporator to produce an orange oil. The oil was rinsed with diethyl ether to form a yellow precipitate. The precipitate was then recrystallized from THF, and washed with chloroform to yield $\text{Si}(\text{DPP})_2$ as a pale yellow solid (130 mg, 17% yield). ^1H NMR ($\text{DMSO}-d_6$, 500 MHz): δ (ppm, relative to TMS) = 6.00 [d, 2H, 7.3 Hz], 6.77 [dd, 2H, 7.3, 7.3 Hz], 6.97 [dd, 2H, 7.3, 7.3 Hz], 8.11 [d, 2H, 7.3 Hz], 8.64, 8.55 [AB₂ pattern, 3H, J_{AB} = 7.7 Hz]. $^{13}\text{C}\{^1\text{H}\}$ NMR ($\text{DMSO}-d_6$,

Table 2
X-ray crystallographic data for **1·½CHCl₃**, **3·THF**, and **3·CHCl₃**.

	1·½CHCl ₃	3·THF	3·CHCl ₃
empirical formula	C _{21.5} H _{17.5} Cl _{1.5} N ₅ Si	C ₃₈ H ₃₀ N ₂ OSi	C ₃₅ H ₂₃ Cl ₃ N ₂ Si
formula weight (g/mol)	427.17	558.73	605.99
crystal system	triclinic	monoclinic	monoclinic
space group, Z	P-1, 4	P2 ₁ /n, 4	P2 ₁ /n, 4
temperature (K)	100	100	100
wavelength (Å)	1.54184	0.71073	0.71073
crystal size (mm)	0.32 × 0.37 × 0.48	0.07 × 0.14 × 0.16	0.08 × 0.09 × 0.14
a, Å	11.1264(3)	12.3940(8)	12.3708(7)
b, Å	12.2430(4)	14.3540(9)	14.0589(9)
c, Å	15.6147(4)	16.3931(13)	16.5093(12)
α, °	82.157(2)	90	90
β, °	86.393(2)	97.736(3)	98.202(3)
γ, °	64.811(3)	90	90
volume (Å ³)	1906.75(10)	2889.8(3)	2841.9(3)
D _{calc} (g/cm ³)	1.488	1.284	1.416
abs. coeff. (mm ⁻¹)	3.176	0.116	0.394
F(000)	884	1176	1248
Θ range for data	4.02–66.81	2.21–26.50	2.41–26.77
reflections collected	33,500	74,489	47,388
data/restraints/parameters	6734 / 0 / 528	5975 / 0 / 379	6031 / 0 / 370
R(int)	0.0321	0.0552	0.0644
final R [I > 2σ(I)] R1, wR2	0.0293, 0.0749	0.0411, 0.0959	0.0397, 0.0924
final R (all data) R1, wR2	0.0321, 0.0773	0.0476, 0.1016	0.0523, 0.1026
goodness-of-fit on F ²	1.031	1.119	1.056
larg. diff. peak, hole, eÅ ⁻³	0.325, -0.346	0.435, -0.304	0.372, -0.510
CCDC Deposition No.	2,109,550	2,109,551	2,109,552

125 MHz): δ (ppm relative to TMS) = 116.2, 123.7, 124.7, 126.5, 130.1, 134.3, 144.0, 152.3, 162.1. ²⁹Si NMR (DMSO-d6, 99 MHz): δ (ppm relative to TMS) = -150.3. Anal. Calc. for C₃₄H₂₂N₂Si: C, 83.92; H, 4.56; N, 5.76. Found: C, 83.74; H, 4.59; N, 5.82%. MS (MALDI-TOF): [M-H]⁺, m/z = 487.7.

All quantum chemical calculations were performed using density functional theory (DFT) [42–45] realized in Gaussian 16 Rev. C.01 program packages. We have performed calculations applying Becke three parameter hybrid functional [46] which uses the non-local correlation provided by the Lee, Yang, and Parr expression [47,48] – B3LYP. As a basis set we have employed standard basis set 6–31C* based on a gaussian type of functions. The combination of functional and basis set was selected based on precision of prediction of the electronic spectrum of silicon hexacoordinated compound Si(bzimpy)₂ using time-dependent DFT approach. For all calculated structures optimized structures were obtained. Frequencies calculations demonstrated absence of negative values indicating that all obtained structures correspond to the global minimum. Single-point energy for structures **3** and the symmetric dimer of **3** were -1707.5683 Hartrees and -3415.134410 Hartrees, respectively (Cartesian coordinates of both species are included in the ESI Tables S7–S8).

Single crystal X-ray diffraction data of **1·½CHCl₃** was acquired with a Rigaku Gemini Ultra diffractometer using Cu K α radiation (λ = 1.5418 Å), while diffraction data of **3·THF** and **3·CHCl₃** were measured using a Bruker D8 Venture diffractometer with Mo K α radiation (λ = 0.71073 Å). Crystals of suitable size were coated with a thin layer of oil, mounted on the diffractometer, and flash cooled to 100 K in a nitrogen cold stream. Data were collected using phi and omega scans. CrysAlisPro [49] and Apex3 [50] software were used to control the diffractometers and perform data reduction. The crystal structures were solved with SHELSX and SHEXL [51]. Alternate cycles of model-building in Olex2 [52] and refinement on F² using full-matrix least squares techniques in SHEXL followed. All non-hydrogen atoms were refined anisotropically. All hydrogen atom positions were calculated based on idealized geometries and recalculated after each cycle of least squares. During refinement, hydrogen atom – parent atom vectors were held fixed (riding motion constraint). Crystallographic data is given in Table 2.

Tables of bond lengths and angles are included in the ESI, Tables S1–S6. Crystallographic data has been deposited with the Cambridge Structural Database, under deposition numbers 2,109,550–2,109,552.

Declaration of Competing Interest

The authors declare the following financial interests which may be considered as potential competing interests. Some of the authors (TS, MW, YZ) are co-inventors on a patent application covering Si(pincer)₂ compounds/complexes and their application in electronic applications, and they are pursuing commercialization of the technology.

Acknowledgments

This research was supported by a grant from the National Science Foundation #1800331. AA and AB acknowledge support from Grant of Ministry of Education and Science of the Republic of Kazakhstan #AP08052504.

Supplementary materials

Supplementary material associated with this article can be found, in the online version, at doi:10.1016/j.jorgchem.2021.122208.

References

- [1] M.G. Voronkov, Silatranes: intra-complex heterocyclic compounds of pentacoordinated silicon, Pure Appl. Chem. 13 (1–2) (1966) 35–59.
- [2] M.G. Voronkov, V.M. D'Yakov, S.V. Kirpichenko, Silatranes, J. Organomet. Chem. 233 (1) (1982) 1–147.
- [3] C.L. Frye, G.A. Vincent, W.A. Finzel, Pentacoordinate silicon compounds. V. Novel silatrane chemistry, J. Am. Chem. Soc. 93 (25) (1971) 6805–6811.
- [4] A. Chandrasekaran, R.O. Day, R.R. Holmes, A new class of silatranes: structure and dynamic NMR behavior, J. Am. Chem. Soc. 122 (6) (2000) 1066–1072.
- [5] J.K. Puri, R. Singh, V.K. Chahal, Silatranes: a review on their synthesis, structure, reactivity and applications, Chem. Soc. Rev. 40 (3) (2011) 1791–1840.
- [6] G. Singh, G. Kaur, J. Singh, Progressions in hyper-coordinate silicon complexes, Inorg. Chem. Commun. 88 (2018) 11–20.

- [7] L.S. Shlyakhtenko, A.A. Gall, A. Filonov, Z. Cerovac, A. Lushnikov, Y.L. Lyubchenko, Silatrane-based surface chemistry for immobilization of DNA, protein-DNA complexes and other biological materials, *Ultramicroscopy* 97 (1–4) (2003) 279–287.
- [8] S. Riggleman, P. DeShong, Application of silicon-based cross-coupling technology to triflates, *J. Org. Chem.* 68 (21) (2003) 8106–8109.
- [9] M.G. Voronkov, Biological activity of silatranes, *Top. Curr. Chem.* 84 (1979) 77–135.
- [10] M.G. Voronkov, V.P. Baryshok, Antitumor activity of silatranes, *Pharm. Chem. J.* 38 (1) (2004) 3–9.
- [11] Recently reviewed in J.E. Pia, B.A. Hussein, V. Skrypac, O. Sarycheva, M.J. Adler, Porphyrin silanes, *Coord. Chem. Rev.* 449 (2021) 214183.
- [12] C.M. Allen, W.M. Sharman, J.E. Van Lier, Current status of phthalocyanines in the photodynamic therapy of cancer, *J. Porphyrins Phthalocyanines* 5 (2) (2001) 161–169.
- [13] M. Lam, N.L. Oleinick, A.L. Nieminen, Photodynamic therapy-induced apoptosis in epidermoid carcinoma cells - Reactive oxygen species and mitochondrial inner membrane permeabilization, *J. Biol. Chem.* 276 (50) (2001) 47379–47386.
- [14] G. Zheng, J. Chen, H. Li, J.D. Glickson, Rerouting lipoprotein nanoparticles to selected alternate receptors for the targeted delivery of cancer diagnostic and therapeutic agents, *Proc. Natl. Acad. Sci. U.S.A.* 102 (49) (2005) 17757–17762.
- [15] J.D. Miller, E.D. Baron, H. Scull, A. Hsia, J.C. Berlin, T. McConnick, V. Colussi, M.E. Kennet, K.D. Cooper, N.L. Oleinick, Photodynamic therapy with the phthalocyanine photosensitizer Pc 4: The case experience with preclinical mechanistic and early clinical-translational studies, *Toxicol. Appl. Pharmacol.* 224 (3) (2007) 290–299.
- [16] H. Kobayashi, P.L. Choyke, Near-infrared photoimmunotherapy of cancer, *Acc. Chem. Res.* 52 (8) (2019) 2332–2339.
- [17] I. Ozturk, A. Tunçel, F. Yurt, Z. Biyiklioglu, M. Ince, K. Ocakoglu, Antifungal photodynamic activities of phthalocyanine derivatives on *Candida albicans*, *Photodiagn. Photodyn. Ther.* 30 (2020) 101705.
- [18] S. Honda, T. Nogami, H. Ohkita, H. Benten, S. Ito, Improvement of the light-harvesting efficiency in polymer/fullerene bulk heterojunction solar cells by interfacial dye modification, *ACS Appl. Mater. Interfaces* 1 (4) (2009) 804–810.
- [19] S. Honda, H. Ohkita, H. Benten, S. Ito, Multi-colored dye sensitization of polymer/fullerene bulk heterojunction solar cells, *Chem. Commun.* 46 (35) (2010) 6596–6598.
- [20] S. Honda, H. Ohkita, H. Benten, S. Ito, Selective dye loading at the heterojunction in polymer/fullerene solar cells, *Adv. Energy Mater.* 1 (4) (2011) 588–598.
- [21] X.F. Qiao, J.C. Zhou, J.W. Xiao, Y.F. Wang, L.D. Sun, C.H. Yan, Triple-functional core-shell structured upconversion luminescent nanoparticles covalently grafted with photosensitizer for luminescent, magnetic resonance imaging and photodynamic therapy in vitro, *Nanoscale* 4 (15) (2012) 4611–4623.
- [22] O.A. Melville, T.M. Grant, B. Mirka, N.T. Boileau, J. Park, B.H. Lessard, Ambipolarity and air stability of silicon phthalocyanine organic thin-film transistors, *Adv. Electron. Mater.* 5 (8) (2019) 1900087.
- [23] T.M. Grant, K.L.C. Kaller, T.J. Coathup, N.A. Rice, K. Hinzer, B.H. Lessard, High Voc solution-processed organic solar cells containing silicon phthalocyanine as a non-fullerene electron acceptor, *Org. Electron.* 87 (2020) 105976.
- [24] B. King, O.A. Melville, N.A. Rice, S. Kashani, C. Tonelle, H. Raboui, S. Swaraj, T.M. Grant, T. McAfee, T.P. Bender, H. Ade, F. Castet, L. Muccioli, B.H. Lessard, Silicon phthalocyanines for n-type organic thin-film transistors: development of structure- property relationships, *ACS Appl. Electron. Mater.* 3 (1) (2021) 325–336.
- [25] C. Breliere, R.J.P. Corriu, G. Royo, W. Man, J. Zwecker, Unexpected reactivity of bifunctional hexacoordinated silicon species, *Organometallics* 9 (10) (1990) 2633–2635.
- [26] C. Breliere, R.J.P. Corriu, G. Royo, J. Zwecker, Hexacoordinate silicon species - A possible model for reaction intermediates.2. Nondissociative permutational isomerization in solution, *Organometallics* 8 (7) (1989) 1834–1836.
- [27] R. Corriu, G. Lanneau, C. Priou, F. Soulairol, R. Probst, R. Conlin, C.Q. Tan, Chemical and photochemical approaches To amino(aryl)silylenes, *J. Organomet. Chem.* 466 (1–2) (1994) 55–68.
- [28] K. Boyer-Elma, F.H. Carre, R.J.P. Corriu, W.E. Douglas, Preparation of a diethynyl hypervalent silicon monomer by coordination-selective cleavage - structure and polymerization to give novel polycarbosilanes containing main-chain hexacoordinate silicon, *J. Chem. Soc., Chem. Commun.* (7) (1995) 725–726.
- [29] M.P. Coles, M.S. Khalaf, P.B. Hitchcock, A new aliphatic N,C,N'-pincer ligand with pendant guanidine groups, *Inorg. Chim. Acta* 422 (2014) 228–234.
- [30] J. Belzner, H. Ihmels, B.O. Kneisel, R.O. Gould, R. Herbstirmer, reactions of a cyclotrisilane with olefins and dienes - evidence for an equilibrium between silylenes and a cyclotrisilane, *Organometallics* 14 (1) (1995) 305–311.
- [31] D.M. Peloquin, D.R. Dewitt, S.S. Patel, J.W. Merkert, B.T. Donovan-Merkert, T.A. Schmedake, Spectroelectrochemistry of tris(bipyridyl)silicon(IV): ligand localized reductions with potential electrochromic applications, *Dalton Trans.* 44 (43) (2015) 18723–18726.
- [32] M. Kocherga, J. Castaneda, M.G. Walter, Y. Zhang, N.A. Saleh, L. Wang, D.S. Jones, J. Merkert, B. Donovan-Merkert, Y.Z. Li, T. Hofmann, T.A. Schmedake, Si(bzimpy)(2) - a hexacoordinate silicon pincer complex for electron transport and electroluminescence, *Chem. Commun.* 54 (100) (2018) 14073–14076.
- [33] J. Song, H. Lee, E.G. Jeong, K.C. Choi, S. Yoo, Organic light-emitting diodes: pushing toward the limits and beyond, *Adv. Mater.* 32 (35) (2020) 1907539.
- [34] N.B. Kotadiya, P.W.M. Blom, G. Wetzelrau, Efficient and stable single-layer organic light-emitting diodes based on thermally activated delayed fluorescence, *Nat. Photonics* 13 (11) (2019) 765–769.
- [35] L.A. Duan, J.A. Qiao, Y.D. Sun, Y. Qiu, Strategies to design bipolar small molecules for OLEDs: donor-acceptor structure and non-donor-acceptor structure, *Adv. Mater.* 23 (9) (2011) 1137–1144.
- [36] W.L. Jia, Q.D. Liu, R.Y. Wang, S.N. Wang, Novel phosphorescent cyclometalated organotin(IV) and organolead(IV) complexes of 2,6-bis(2'-indolyl)pyridine and 2,6-bis[2'-(7-azaindolyl)]pyridine, *Organometallics* 22 (20) (2003) 4070–4078.
- [37] R.A. Marcus, N. Sutin, Electron transfers in chemistry and biology, *Biochim. Biophys. Acta* 811 (3) (1985) 265–322.
- [38] V. Coropceanu, J. Cornil, D.A. da Silva, Y. Olivier, R. Silbey, J.L. Bredas, Charge transport in organic semiconductors, *Chem. Rev.* 107 (4) (2007) 926–952.
- [39] Q. Xiao, X.T. Meng, M. Kanai, Y. Kuninobu, Palladium-catalyzed C–H fluorosilylation of 2-phenylpyridines: synthesis of silafluorene equivalents, *Angew. Chem. Int. Ed.* 53 (12) (2014) 3168–3172.
- [40] S. Furuta, T. Mori, Y. Yoshigoe, K. Sekine, Y. Kuninobu, Synthesis, structures and photophysical properties of hexacoordinated organosilicon compounds with 2-(2-pyridyl)phenyl groups, *Org. Biomol. Chem.* 18 (17) (2020) 3239–3242.
- [41] R.M. Wan, J.A. Buss, K.T. Horak, T. Agapie, A hemilabile diphosphine pyridine pincer ligand: sigma- and pi-binding in molybdenum coordination complexes, *Polyhedron* 187 (2020) 114631.
- [42] R.G. Parr, W. Yang, Density-functional theory of atoms and molecules, Oxford Univ. Press, Oxford, 1989.
- [43] D.R. Salahub, M.C. Zerner, The challenge of d and f electrons: theory and computation, American Chemical Society, Washington D.C., 1989.
- [44] W. Kohn, L.J. Sham, self-consistent equations including exchange and correlation effects, *Phys. Rev.* 140 (1965) A1133.
- [45] P. Hohenberg, W. Kohn, Inhomogeneous electron gas, *Phys. Rev.* 136 (1964) B864.
- [46] A.D. Becke, Density-functional thermochemistry. III. The role of exact exchange, *J. Chem. Phys.* 98 (1993) 5648–5652.
- [47] C. Lee, W. Yang, R.G. Parr, Development of the Colle-Salvetti correlation-energy formula into a functional of the electron density, *Phys. Rev. B* 37 (2) (1988) 785–789.
- [48] B. Miehlich, A. Savin, H. Stoll, H. Preuss, Results obtained with the correlation-energy density functionals of Becke and Lee, Yang and Parr, *Chem. Phys. Lett.* 157 (3) (1989) 200–206.
- [49] Rigaku Oxford DiffractionCrysAlisPro Software System, Version 1.171.38.46, Rigaku Corporation, Oxford, UK, 2018.
- [50] APEX 3APEX 3, v2017.3, Bruker-AXS Inc., Madison, WI, 2017.
- [51] G.M. Sheldrick, A short history of SHELX, *Acta Crystallogr. A* 64 (2008) 112–122.
- [52] O.V. Dolomanov, L.J. Bourhis, R.J. Gildea, J.A.K. Howard, H. Puschmann, OLEX2: a complete structure solution, refinement and analysis program, *J. Appl. Cryst.* 42 (2009) 339–341.